

Self-Propulsion of floating ice blocks caused by melting in water

Michael Berhanu^{*}, Amit Dawadi[†], Martin Chaigne^{*}, Jérôme Jovet[§] and Arshad Kudrolli[†]

^{*} *MSC, Université Paris Cité, CNRS (UMR 7057), F-75013 Paris, France*

[§] *Physics Department, Université Paris Cité, F-75013 Paris, France and*

[†] *Department of Physics, Clark University, Worcester, Massachusetts*

(Dated: December 23, 2024)

We show that floating ice blocks with asymmetric shapes can self-propel with significant speeds due to buoyancy driven currents caused by the melting ice. Model right-angle ice wedges are found to move in the direction opposite to the gravity current which descends along the longest inclined side in water, with temperatures above 4°C. We describe the measured speed as a function of the length and angle of the inclined side, and the temperature of the bath in terms of a propulsion model which incorporates the cooling of the surrounding fluid by the melting ice. We show the heat pulled from the surrounding liquid by the melting ice block leads to net propulsion which is balanced by drag. We further show that the ice block moves robustly in a salt water bath with salinity similar to that of the ocean, in the same direction as in fresh water, implying that this propulsion mechanism may be relevant to icebergs in sufficiently warm oceans.

The melting of icebergs floating on the ocean is often accompanied by buoyant convection flows [1], as local temperature and salinity variations modify the water density. Consequently, significant gravity driven currents occur below the water surface in the vicinity of icebergs. These currents carry momentum and as a result can lead to iceberg motion in addition to the important contribution of the wind, surface waves, oceanic currents and Coriolis force [2–5]. This idea has been proposed by Mercier, *et al.* [6] as a perspective to their work in which they demonstrated the self-propulsion of a floating asymmetric solid with an embedded local heat source that generates thermal convection. In the case of a melting block in a bath at a temperature higher than the melting temperature, an added source of energy is not required to create a heat flux and convection currents. Previously, Dorbolo, *et al.* related the spinning of floating ice disks to the convection flow driven by melting [7]. No translation was reported because the disks were symmetric and were constrained to rotate by fixing the center position using magnets. Recently, it was demonstrated that a boat incorporating an inclined solute material like salt or sugar can propel more rapidly due to the solutal convection flow driven by the dissolution [8]. We build on that study by investigating the case of asymmetric ice blocks, which melt in warm water. In contrast to the dissolution of salt and sugar, which are denser than the water bath, a buoy is not needed to ensure flotation, as ice floats on water (density $\rho_{ice} = 916.7 \text{ kg m}^{-3} < \rho_{water} = 999.8 \text{ kg m}^{-3}$ at the melting temperature $T_m = 0^\circ\text{C}$ [9]).

Here, we investigate the kinematics of ice blocks which have asymmetric shapes while floating in a water bath and show that they can not only rotate but translate with significant speeds. We find a typical propulsion velocity of about 3 mm s^{-1} for triangular ice prisms with an inclined long side of approximately 20 cm and width of approximately 10 cm, floating in a water bath held at a temperature of about $T_b = 22^\circ\text{C}$. We use a shadowgraph

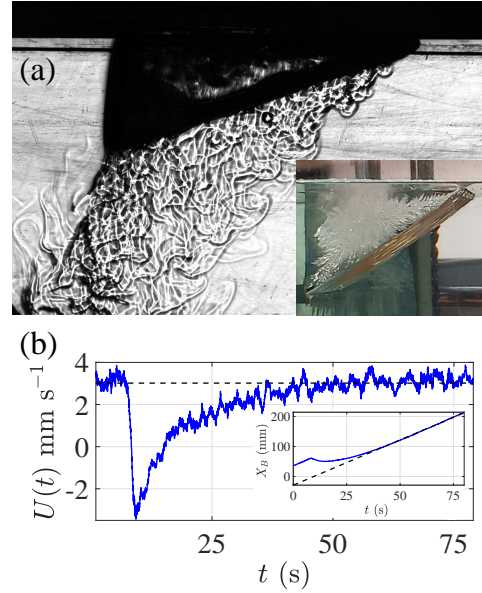


FIG. 1. (a) Shadowgraph image of the convection flow around an ice block. The flow is directed toward the rear of the block, while the block is propelled in the opposite direction (see Movie S1 in SM). Inset: Image of a right-angle ice wedge. (b) The horizontal velocity of the block U as a function of time t . The block is kicked manually in the direction opposite to the motion induced by propulsion at $t = 8 \text{ s}$. After a transient, the block recovers and reaches the same velocity $U_b = 3.02 \text{ mm s}^{-1}$ indicated by the dashed line. Inset: The horizontal position of the immersed part of the block $X_B(t)$. Dashed line: linear fit.

imaging setup [10, 11] to simultaneously track the motion of the block and visualize the buoyancy convection flow. A phenomenological model relating the melting rate to the terminal speed is developed to explain the magnitude of the observed ice block translation velocities as a function of their size, inclination, and bath temperature. Although latent heat plays an important role in the dynamics and determines the time over which the block

melts, its actual magnitude does not significantly affect the propulsion speeds according to our model. This is because the heat required to raise the temperature of the ice block to the melting temperature is relatively small. We then go on to demonstrate experimentally that the melting-driven propulsion mechanism remains functional when the bath salinity is increased to that of oceans, suggesting its possible relevance to icebergs in sufficiently warm oceans.

We cast asymmetric ice blocks with a simple geometry: a prism with a rectangular triangle that has a hypotenuse of length L and inclined w.r.t the horizontal by an angle θ . Various sizes over ten centimeters in scale were studied (see list in Supplementary Material [12] (SM) Section III). Then, the blocks are delicately positioned with the right angle on top, in a water bath of a few hundred liters. The ice block and its motion in the tank are either observed from the side using a shadowgraph imaging (see Fig. 1 (a)) or from the top (see SM Sec. III). Because cooled water is denser than the surrounding bath, a thermal convection flow develops below the melting block after a transient of a few tens of seconds. From the shadowgraphs, we observe that this flow detaches and follows the inclined side of the block, creating a current from the tip at the front towards the back. Consequently, by reaction, the wedge shaped block moves in the opposite direction (see SM MovieS1). However, the movement is not exactly rectilinear, but includes rotation to a small degree. This rotation motion is analogous to the spinning of symmetric ice disks [7, 13] and is caused by the destabilization of the falling convection flow into a vortex. While the sides of the block melt at a rate of a few ten microns per second, we observe that the block inclination is approximately conserved at least during the first ten minutes, even though it shrinks and the edges round over time. After about ten minutes, the relative magnitude of the spinning motion becomes increasingly important before the block completely melts.

After a transient of few tens of seconds, the ice block reaches a terminal velocity when the propulsion force balances the drag. We measure the block displacement X_B by thresholding the images, and obtain the terminal velocity U_b by fitting a line to the horizontal position as shown in the inset to Fig. 1(b). The instantaneous velocity $U(t)$ is computed over a moving 1 s time interval in Fig. 1(b). As illustrated, the forward motion is quite robust. When a moving block is manually kicked to move in the opposite direction, it accelerates and reaches the pre-kick horizontal velocity $U_b \approx 3.02 \text{ mm s}^{-1}$ in about 30 s. We also observe the emergence of concave grooves surrounded by crests along the inclined side (see SM Sec. IV). This melting pattern is a generic feature of ablation [14] and is likely caused by the convection plumes advected by the mean current. Such grooves have been also reported in simulations [15]. Nonetheless, these patterns do not appear to affect the robustness of the trans-

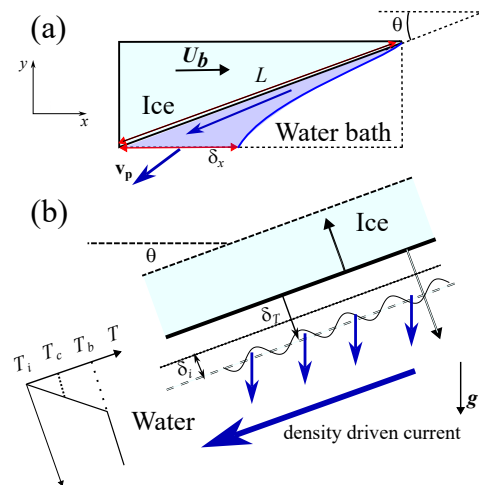


FIG. 2. (a) Schematic of the propulsion mechanism. The time average convection current of velocity v_p escaping from the control volume below the ice block on a length δ_x generates a horizontal thrust in the opposite direction. In stationary regime, this thrust balances the fluid drag. (b) Melting mechanism of an inclined ice block above water driven by thermal convection.

lation motion.

The terminal velocities were measured using a few hundred wedge ice blocks while varying the bath temperature T_b , the block underside inclination angle θ and length L (see SM Sec. III). We observe that symmetric rectangular ice blocks do not have a net translation motion (see also SM Section III). The values show significant experimental variability compared with dissolution propelled boats [8] that we attribute to several factors. The typical scale of the plumes is larger compared to the block size leading to greater fluctuations in their trajectories. The shapes of the ice blocks are not perfectly flat and reproducible to only about 5% variation. The ice block releases trapped bubbles during melting that further perturb the flow. Nonetheless, we observe a robust directed motion with a block velocity of $U_b \approx 3 \text{ mm s}^{-1}$ which is easily noted with the naked eye for a wedge ice block of about 20 cm long melting in a bath at 22°C . The corresponding Reynolds number built on the block size $Re = \frac{L U_b}{\nu}$ is of order 600, with the kinematics viscosity of water $\nu \approx 10^{-6} \text{ m}^2 \text{ s}^{-1}$. Thus, the ice block moves in the inertial regime, and we propose a phenomenological model inspired by Chaîne, *et al.* [8] to explain our observations.

We propose a 2D modeling in the plane shown in Fig. 10(a). According to Ref. [8], the horizontal propulsion force F_p can be evaluated by a momentum balance on a control volume below the inclined wall. We do not take into account the nearly vertical back surface as we did not observe significant water motion near that surface. We neglect also the lateral flat sides, which do not generate a net propulsion contribution by symmetry. The time average current below the block of velocity v_p

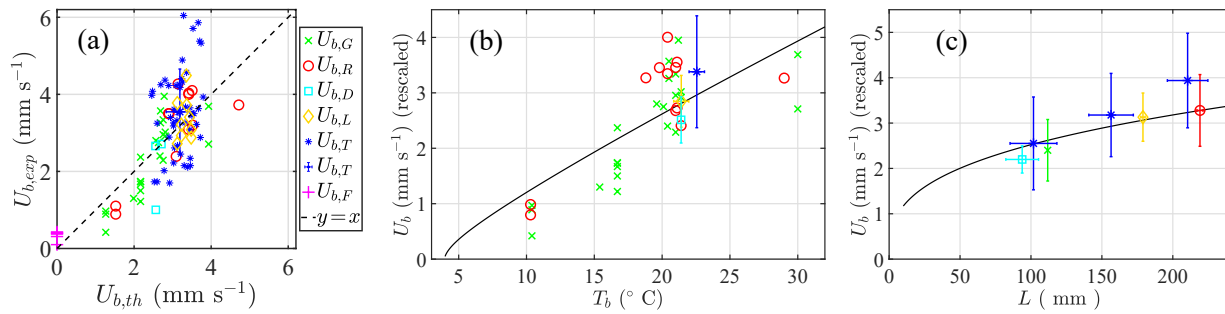


FIG. 3. (a) Measured terminal velocity $U_{b,exp}$ as a function of the theoretical estimate $U_{b,th}$ in a fresh water bath. Despite the significant experimental dispersion, the measured U_b are consistent with the model. (b) $U_{b,exp}$ as a function of the bath temperature T_b and comparison with model $U_{b,th}$ (black line). (c) $U_{b,exp}$ as a function of the ice block inclined length L . The values of $U_{b,exp}$ are rescaled in (b-c), according to the theoretical model in order to compare experiments with different block properties. Data sets for $U_{b,exp}$ (see SM Sec. III). $U_{b,G}$, dim. $100 \times 100 \times 50$ mm³, $\theta \approx 24^\circ$, variable temperature. $U_{b,R}$, $L \approx 21$ cm, variable temperature and inclination. $U_{b,D}$, clear ice, approx. dim. $100 \times 40 \times 40$ mm³. $U_{b,L}$, clear ice, approx. dim. $165 \times 125 \times 65$ mm³. $U_{b,T}$, view from the top, variable dimensions and inclinations. The error bars show the average value and \pm the standard deviation. $U_{b,F}$, clear ice, rectangular blocks dim. $100 \times 40 \times 40$ mm³, $\theta \approx 0^\circ$. Only displayed in (a) and we find $U_b \approx 0$. Except for $U_{b,T}$, the measurements have been extracted from shadowgraph experiments. (c) The dataset for $U_{b,T}$ is divided into three subranges in L to better visualize the influence of L , while maintaining statistical averaging.

generates a horizontal thrust which is balanced by an inertial drag. Consequently, the boat terminal velocity U_b is evaluated to first order [8],

$$U_{b,th} = \sqrt{\frac{\sin 2\theta \delta_x}{2C_d L_A}} v_p, \quad (1)$$

where C_d is the drag coefficient of the ice block of order one, which we assume to be 0.6 because of geometric similarity with those studied previously [8], the projected length $L_A \approx L \sin \theta$, and the distance over which the flow is ejected from the volume $\delta_x = \frac{1}{2} \cos^2 \theta L$. However, significant differences arise in the calculation of v_p generated by the ice melting in the water bath versus those for dissolution calculated previously [8] (see SM Sec. VIII).

In Fig. 10 (b), we consider the melting of an ice interface, which is inclined at an angle θ to the horizontal and in contact with the water bath at a temperature T_b , above the temperature of maximal water density at $T_c = 3.98 \approx 4^\circ$ C. As we observe a strong convection flow below the melting ice block in Fig. 1(a), we assume that the ice melting is driven by thermal convection. This regime has been previously noted by Kerr in Appendix B of Ref. [16] and characterized with simulations and experiments in the region below a horizontal ice slab by Keitzl, *et al.* [17]. Here, we derive a more direct model which gives the same scaling law (see SM Sec. VIII) using Bigg's relation for density as a function of temperature $\rho(T)$ [18]. In stationary regime, the thermal boundary layer has a constant thickness δ_T and we assume a linear temperature profile between the ice melting temperature $T_i = T_m = 0^\circ$ C and the bath temperature T_b (see Fig. 10). However, only a width δ_i , where $T > T_c$, can be unstable with respect to gravity, if it is sufficiently thick. In the stationary regime, the value of δ_i is given by the criterion for constant

Rayleigh number [19–22]. The Rayleigh number is defined as $Ra = (\Delta\rho g \cos \theta \delta_i^3)/(\rho \kappa \nu)$, where $g = 9.81$ m s⁻² is the gravitational acceleration and $\kappa \approx 1.33 \times 10^{-7}$ m² s⁻¹ is the thermal diffusivity of water. Then, Ra has the value at marginal instability, that is $Ra_c = 27/4 \pi^4$ for a layer between two fluids [23]. Then, δ_T is deduced from δ_i as the temperature profile is linear.

The melting rate is calculated by approximating the Stefan condition [24],

$$v_m = \Gamma \frac{\rho(T_i)}{\rho_i} \frac{C_p \kappa}{\mathcal{L}} \frac{(T_c - T_i)}{\delta_i}, \quad (2)$$

where C_p is the heat capacity of liquid water, ρ_i is the ice density and \mathcal{L} is the melting latent heat per mass unit, Γ is a fitting constant. Keitzl *et al.* [17] find a similar scaling law using a more complex reasoning. Complementary experiments were performed to calibrate the melting rate in our experiment (see SM Appendix Sec. IX) and found $\Gamma = 2.187$. The heat extracted from the bath to melt the ice corresponds to a cooling of the bath between the front and the back of the ice block. Consequently, the cooler and denser water at the back drives the average gravity current velocity v_p since it is balanced by inertial friction, enabling us to determinate v_p from v_m (see Eq. (S15) in SM Sec. VIII).

We compare the prediction of our model $U_{b,th}$ with experimental measurements $U_{b,exp}$ in Fig. 3(a). We find that they are broadly in agreement in spite of the significant experimental variations and theoretical assumptions. In Fig. 3(b), $U_{b,exp}$ is plotted as a function of the bath temperature T_b . The model is observed to capture the observed large decrease in speed at lower temperatures. The comparison of U_b as a function of L is shown in Fig. 3(c), and is observed to be well captured by the model.

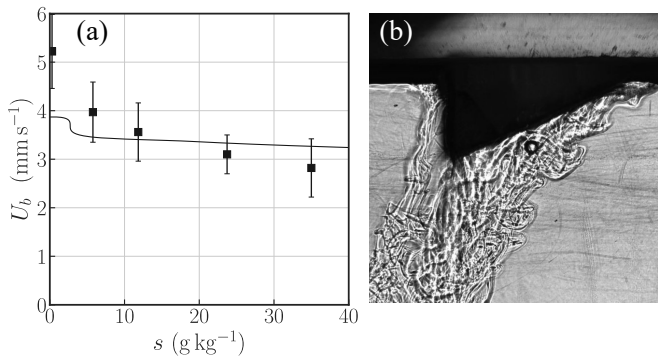


FIG. 4. (a) Measured terminal velocity $U_{b,exp}$ as a function of the salinity (square markers). $T_b \approx 23^\circ \text{C}$, $L \approx 210 \text{ mm}$ and $\theta \approx 25^\circ$. Line, theoretical estimate $U_{b,thS}$, according to the modified model in salt water (see SM Sec. X). (b) Shadowgraph image of an ice block moving in salt water (salinity 31 g kg^{-1}). Block dim. $100 \times 100 \times 50 \text{ mm}^3$, $T_b = 24.6^\circ \text{C}$, $U_b = 2.28 \text{ mm s}^{-1}$. (See MovieS4 in SM).

Finally, we investigate if ice blocks move in salt water with salinity up to that of oceans, and in which direction. The oceans have a salinity of about 35 g per kg of seawater, and thus the physics of ice melting in oceans is considerably different than in fresh water [25]. Salinity changes the water density more strongly in comparison with variations due to temperature besides decreasing T_m . To test the influence of bath salinity on the propulsion mechanism studied here, a set of experiments with visualization from the top were performed. Fig. 4(a) shows the measured speed of the ice blocks (square markers) in salt water baths where the salinity has been varied between that of fresh water and that of ocean water and for temperatures about 23°C . We observe that the velocity drops systematically as the salinity is increased to that of ocean water. Interestingly the direction of propulsion remains the same as in fresh water, counter to the intuition that melted fresh water should rise in saltwater.

To visualize the mechanism, we examine the flow below the ice using shadowgraph imaging. In Fig. 4(b), we observe a convection flow below the melting block, similar to the descending plumes observed in fresh water. Thus, we find that the contribution of convection due to the cooling of the surrounding salt bath dominates the rising cold fresh water near the melting surface. We show evidence of this by adding dye to the ice and observing that the resulting meltwater can be found at the top (See SM Fig. S9). Fig. 4(a) shows a comparison of the measured and theoretical value of U_b , after including in the model the opposing effect of melt water flow up the incline in addition to the forward propulsion due to cold water descending behind the ice block (see SM Sec. X). We find a reasonable agreement showing that the underlying propulsion mechanism observed in ice blocks melting in fresh water is also applicable to those melting in salt water.

Building on previous work on propulsion due to solutal convection, we have demonstrated experimentally that asymmetric floating ice blocks melting in water self-propel at least for sufficiently high bath temperatures. The propulsion phenomenon studied here is robust and is not strongly dependent on the exact dimensions of the ice block, of its rounding and of its encapsulated air fraction. We have neglected the change of shape during the melting, because experimentally the inclination does not change during the first half of the lifetime of a block.

Icebergs found in the Atlantic ocean are typically about one hundred meters in scale, irregular shaped and composed of frozen fresh water, produced by the calving of ice sheets around Antarctica and Greenland [1]. Since icebergs can drift thousand of kilometers towards the equator and reach warm waters with temperature above 4°C , the propulsion mechanism discussed in our study may be relevant to icebergs. We also stated in Chaigne *et al.* [8] in the discussions, that the presence of currents generated by melting is sufficient to generate a significant propulsion. Evidence of these currents in the field [1, 26, 27] supports the relevance of this mechanism for some icebergs, although it is difficult to relate the thrust to the environmental and iceberg properties.

Further, we have assumed that the melt layer remains laminar and is not mixed with the bath by the turbulence of the flow which means that its composition is entirely made of fresh water which consequently does not affect T_m of this ice. While this assumption may be reasonable for centimeter scale ice blocks, it is likely to break down at longer length scales. Indeed, models of kilometer ice shelves consider turbulent boundary layers [28], but these models are not yet supported by in situ measurements. These issues point to a need for further experimental study of ice melting in water with temperatures approaching T_m .

We acknowledge Sylvain Courrech du Pont and Philippe Brunet at MSC, Université Paris Cité for scientific discussions and technical help. M.B. and M. C. are supported by French Research Council project through grant *PhysErosion ANR-22-CE30-0017*.

-
- [1] C. Cenedese and F. Straneo, Annual Review of Fluid Mechanics **55**, 377 (2023).
 - [2] D. G. Mountain, Cold Regions Science and Technology **1**, 273 (1980).
 - [3] L. E. Andersson, F. Scibilia, and L. Imsland, Cold Regions Science and Technology **131**, 88 (2016).
 - [4] T. J. Wagner, R. W. Dell, and I. Eisenman, Journal of Physical Oceanography **47**, 1605 (2017).
 - [5] A. Marchenko, N. Diansky, and V. Fomin, Applied Ocean Research **88**, 210 (2019).
 - [6] M. J. Mercier, A. M. Ardekani, M. R. Allshouse,

- B. Doyle, and T. Peacock, *Phys. Rev. Lett.* **112**, 204501 (2014).
- [7] S. Dorbolo, N. Adami, C. Dubois, H. Caps, N. Vandewalle, and B. Darbois-Textier, *Phys. Rev. E* **93**, 033112 (2016).
- [8] M. Chaigne, M. Berhanu, and A. Kudrolli, *Proceedings of the National Academy of Sciences* **120**, e2301947120 (2023).
- [9] D. R. Lide, ed., *The Handbook of Chemistry and Physics* (CRC Press, 2004).
- [10] G. S. Settles, *Schlieren and shadowgraph techniques: visualizing phenomena in transparent media* (Springer Science & Business Media, 2001).
- [11] G. S. Settles and M. J. Hargather, *Measurement Science and Technology* **28**, 042001 (2017).
- [12] See Supplemental Material at xxxxxx for further information on movies and analysis, which includes Refs. [29–33].
- [13] L. M. Schellenberg, T. J. Newton, and G. R. Hunt, *Environmental Fluid Mechanics* **23**, 465 (2023).
- [14] M. Chaigne, S. Carpy, M. Massé, J. Derr, S. Courrech du Pont, and M. Berhanu, *Proceedings of the National Academy of Sciences* **120**, e2309379120 (2023).
- [15] L.-A. Coustou, E. Hester, B. Favier, J. R. Taylor, P. R. Holland, and A. Jenkins, *Journal of Fluid Mechanics* **911**, A44 (2021).
- [16] R. C. Kerr, *Journal of Fluid Mechanics* **280**, 287 (1994).
- [17] T. Keitzl, J.-P. Mellado, and D. Notz, *Journal of Physical Oceanography* **46**, 1171 (2016).
- [18] P. Bigg, *British Journal of Applied Physics* **18**, 521 (1967).
- [19] W. R. Malkus, *Proceedings of The Royal Society A* **225**, 196 (1954).
- [20] T. S. Sullivan, Y. Liu, and R. E. Ecke, *Phys. Rev. E* **54**, 486 (1996).
- [21] J. Philippi, M. Berhanu, J. Derr, and S. Courrech du Pont, *Phys. Rev. Fluids* **4**, 103801 (2019).
- [22] C. Cohen, M. Berhanu, J. Derr, and S. Courrech du Pont, *Phys. Rev. Fluids* **5**, 053802 (2020).
- [23] S. Chandrasekhar, *Hydrodynamic and Hydromagnetic Stability* (Clarendon Press, Oxford, 1961).
- [24] V. Alexiades and A. D. Solomon, *Mathematical modeling of melting and freezing processes* (Taylor & Francis, 1993).
- [25] A. L. McCutchan and B. A. Johnson, *Journal of Marine Science and Engineering* **10**, 1008 (2022).
- [26] J. J. Helly, R. S. Kaufmann, G. R. Stephenson, and M. Vernet, *Deep Sea Research Part II: Topical Studies in Oceanography* **58**, 1346 (2011), free-Drifting Icebergs in the Southern Ocean.
- [27] A. E. Yankovsky and I. Yashayaev, *Deep Sea Research Part I: Oceanographic Research Papers* **91**, 1 (2014).
- [28] A. Malyarenko, A. J. Wells, P. J. Langhorne, N. J. Robinson, M. J. Williams, and K. W. Nicholls, *Ocean Modelling* **154**, 101692 (2020).
- [29] E. G. Josberger, *Journal of Physical Oceanography* **10**, 474 (1980).
- [30] Y. Du, Z. Wang, L. Jiang, E. Calzavarini, and C. Sun, *Journal of Fluid Mechanics* **960**, A35 (2023).
- [31] B. Castaing, G. Gunaratne, F. Heslot, L. Kadanoff, A. Libchaber, S. Thomae, X.-Z. Wu, S. Zaleski, and G. Zanetti, *Journal of Fluid Mechanics* **204**, 1 (1989).
- [32] G. Ahlers, S. Grossmann, and D. Lohse, *Reviews of modern physics* **81**, 503 (2009).
- [33] T. J. McDougall and P. M. Barker, *Scor/iapso WG127* **127**, 1 (2011).

Supplemental Material: Self-Propulsion of floating ice blocks caused by melting in water

Movies

- **MovieS1.mp4.** Shadowgraph imaging of a self-propelled ice block floating in fresh water. The playback frame rate has been increased by 5. Block dimensions: $L_h \times W \times H = 163 \times 124 \times 65 \text{ mm}^3$, inclination angle $\theta = 19.5^\circ$, bath temperature $T_b = 22^\circ \text{ C}$.
- **MovieS2.mp4.** Shadowgraph imaging of a self-propelled ice block floating in fresh water. The playback frame rate has been increased by 5. Block dimensions $L_h \times W \times H = 100 \times 100 \times 50 \text{ mm}^3$, inclination angle $\theta = 24^\circ$, bath temperature $T_b = 21.4^\circ \text{ C}$.
- **MovieS3.mp4.** Shadowgraph imaging of a clear ice block floating in fresh water. Without inclination, no consistent directed motion is observed and the rotation motion of the block becomes dominant towards the end of the melting process. Two overturning, or capsizing events can be observed, which significantly affects the convection flow. Capsizing are not observed in wedge ice blocks. The playback frame rate has been increased by 5. Rectangular shape. Dimensions $L_h \times W \times H = 100 \times 100 \times 40 \text{ mm}^3$, inclination angle $\theta = 0^\circ$, bath temperature $T_b = 20.1^\circ \text{ C}$.
- **MovieS4.mp4.** Shadowgraph imaging of a self-propelled ice block floating in salt water. The playback frame rate has been increased by 5. Dimensions $L_h \times W \times H = 100 \times 100 \times 50 \text{ mm}^3$, inclination angle $\theta = 24^\circ$, bath temperature $T_b = 24.6^\circ \text{ C}$. Salinity: 31 g of salt per kg of water.

Experimental methods

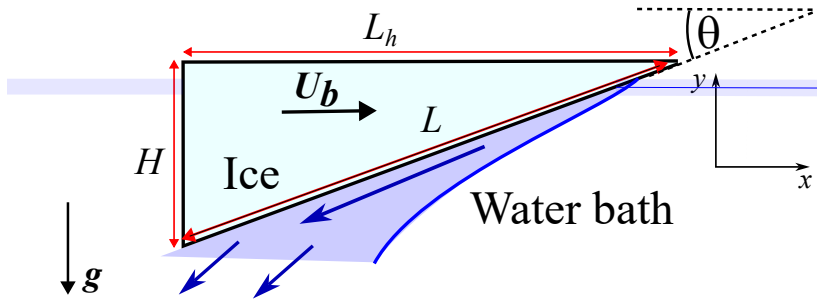


FIG. 5. Schematic of a melting ice block self-propelling while floating in water. The ice blocks are cast as right angle triangle prisms of width W sides H and L_h . The hypotenuse has a length L and is inclined at an angle θ relatively to the horizontal. The ice blocks propels along the horizontal coordinate x at steady state with a terminal velocity U_b . The actual hypotenuse inclination angle differs from θ by few degrees due to the buoyancy equilibrium of the asymmetric block (see Sec.).

We built asymmetric ice blocks by filling filtered demineralized water in molds of prescribed shape and freezing them at -15°C . We choose a right angle triangle prism as a model that has a hypotenuse of length L and is inclined at an angle θ with respect to the horizontal (see Fig. 5). Approximately one hundred blocks were cast with various sizes over the range of a few tens of centimeters. No particular care was taken to produce bubble-free ice blocks which typically results in about 10% of air by volume, similar to icebergs [29]. A few clear rectangular ice blocks were obtained from the Nice company (<https://www.thenicecompanyparis.com/fr>). These blocks are nearly transparent and defect-free. The rectangular blocks were cut into triangular prisms with a hot wire. The various data sets corresponding to a particular ice block kind are listed in Section . Experiments performed with the clear ice blocks, without any trapped bubbles, were found to give the same results.

Prior to the commencement of an experiment, an ice block is left to rest at ambient temperature (about 20°C) for about ten minutes in order to avoid thermal shocks when plunging it into the bath. During this time, the ice temperature approaches the melting temperature. Then, the block is carefully placed with its right angle on the top in a water bath with dimensions that are large compared to the block size. The flotation equilibrium corresponds to the vertical alignment of the gravity center and the center of the immersed part and is typically reached after few oscillations over a few seconds. For this block geometry, at equilibrium, the hypotenuse is immersed in the fluid, whereas the second largest side of the right triangle emerges above the surface. This leads to a systematic difference of a few degrees between θ and the block hypotenuse inclination angle with respect to the horizontal. As shown numerically in Sec. 8, inclinations larger than 39.6° are unstable.

The ice blocks and their motion in the bath are either observed from the top with a camera or from the side using a shadowgraph imaging. In the experiments viewed from the top, we use a glass tank with dimensions $90.5 \times 44.5\text{ cm}^2$, filled up to a height of at least 25 cm with filtered water corresponding to a volume of about 100 liters. To observe the dynamics with shadowgraphy, we use a glass tank with dimensions $116 \times 46\text{ cm}^2$ filled up to 24 cm with tap water corresponding to a volume of about 128 liters. A small Light Emitting Diode (LED) located at the focus of a parabolic mirror (diameter 406 mm and focal length 1800 mm) is used for illumination, and a digital camera is located at focus of the mirror by the means of a semi-reflective plate. The glass tank with the melting ice block is located close to the mirror. The resulting light beam with nearly parallel rays is diverted by the variations of optical indices due to temperature variations. Thus, these regions appear darker. In the shadowgraph images, the convection plumes (colder and thus denser) than the bath appear more clearly in the images than with ambient light imaging. This two-dimensional imaging integrates the density variations along the width of the tank.

In the shadowgraph experiments, two nylon threads (1 mm in diameter) are positioned just below the surface, parallel to this side and separated by a distance slightly greater than the width of the ice block, to guide the motion of the ice block. They maintain the distance between the block and the camera and limit the rotation effect, facilitating observations.

Data sets

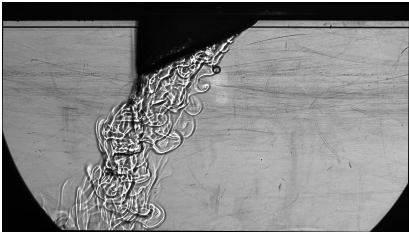
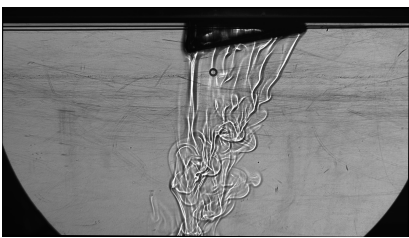
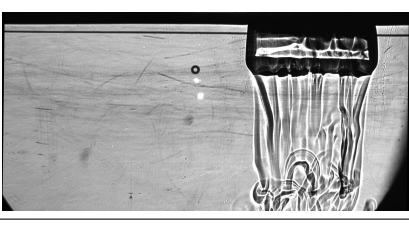
| Data Set | Image example | $L_h \times W \times H$ (mm ³) | L (mm) | θ (°) | Comments and Visualization | U_b mm s ⁻¹ |
|---------------------|---|--|---------------------------------|------------------------------------|--|----------------------------------|
| G 27 runs |  | 100 × 100 × 50 | 112 | 24.3 | Custom made silicon molds. $10.4 \leq T_b \leq 30^\circ$ C. Shadowgraph | Avg. 2.3 range [0.4, 4.0] |
| R 12 runs |  | Typical-size 210 × 85 × 60 | Avg. 220 range [216, 222] | Avg. 12.5 range [8, 15.8] | Inclined silicon molds partially filled. Variable dimensions. $10.3 \leq T_b \leq 29^\circ$ C. Shadowgraph. | Avg. 3.1 range [0.9, 4.3] |
| D 4 runs |  | Typical-size 100 × 100 × 40 | Avg. 94 range [79, 106] | Avg. 15.2 range [12, 17.2] | Rectangular clear ice blocks cut in two along the diagonal using a hot wire. No trapped air. $T_b = 21.4^\circ$ C Shadowgraph | Avg. 2.4 range [2.0, 2.7] |
| L 9 runs |  | Typical-size 165 × 125 × 65 | Avg. 179 range [176, 180] | Avg. 15.7 range [11.8, 19.4] | Rectangular ice blocks cut in two along the diagonal using a hot wire. Low content in air. $20.9 \leq T_b \leq 22.1^\circ$ C. Shadowgraph | Avg. 3.36 range [2.7, 4.5] |
| F 6 runs |  | 100 × 100 × 40 | 100 | 0 | Clear ice. Rectangular ice blocks. No trapped air. $20.4 \leq T_b \leq 21.4^\circ$ C. Shadowgraph | Avg. 0.3 range [0.1, 0.43] |
| T 47 runs |  | Typical-size 160 × 130 × 60 | Avg. 163 range [72, 235] | Avg. 19.5 range [6, 36] | Inclined silicone molds partially filled. Variable dimensions. $22 \leq T_b \leq 24^\circ$ C. Top view | Avg. 3.5 range [1.7, 6.0] |

TABLE I. List of various data sets for experiments performed in a fresh water bath.

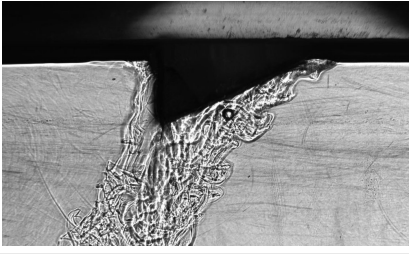
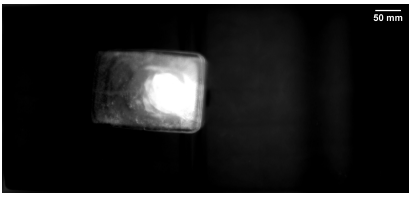
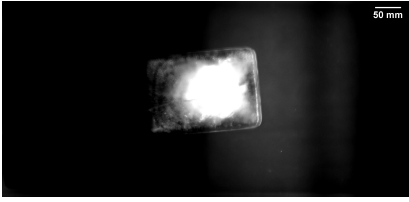
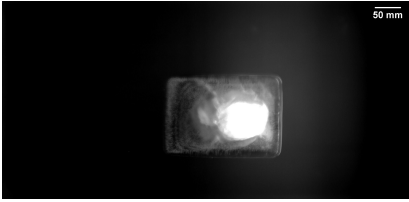
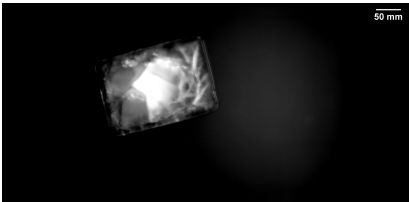
| Data Set | Image example | $L_h \times W \times H$ (mm ³) | L (mm) | θ (°) | Comments and Visualization | U_b mm s ⁻¹ |
|---------------------------------|---|--|---------------------------------|--------------------------------|--|---------------------------------|
| G_s 8 runs |  | 100 × 100 × 50 | 112 | 24.3 | Salinity 31 g kg ⁻¹ Custom made silicon molds. 21.7 ≤ T_b ≤ 24° C. Shadowgraph | Avg. 1.9 range [1.2, 2.5] |
| T_s1 7 runs |  | Typical-size 210 × 130 × 100 | Avg. 234 range [222, 249] | Avg. 26 range [6, 36] | Salinity 5.8 g kg ⁻¹ Inclined silicone molds partially filled. Variable dimensions. 22 ≤ T_b ≤ 24° C. Top view | Avg. 4.0 range [3.3, 4.9] |
| T_s2 9 runs |  | Typical-size 210 × 130 × 100 | Avg. 220 range [206, 234] | Avg. 23 range [22, 24] | Salinity 11.8 g kg ⁻¹ Inclined silicone molds partially filled. Variable dimensions. 22 ≤ T_b ≤ 24° C. Top view | Avg. 3.6 range [2.8, 4.5] |
| T_s3 8 runs |  | Typical-size 210 × 130 × 100 | Avg. 220 range [209, 235] | Avg. 23.3 range [23, 24] | Salinity 23.7 g kg ⁻¹ Inclined silicone molds partially filled. Variable dimensions. 22 ≤ T_b ≤ 24° C. Top view | Avg. 3.1 range [2.8, 3.7] |
| T_s4 7 runs |  | Typical-size 210 × 130 × 100 | Avg. 217 range [199, 232] | Avg. 23 range [23, 24] | Salinity 35 g kg ⁻¹ Inclined silicone molds partially filled. Variable dimensions. 22 ≤ T_b ≤ 24° C. Top view | Avg. 2.8 range [2.4, 3.5] |

TABLE II. List of various data sets for experiments performed in a salt water bath.

Ice surface grooves

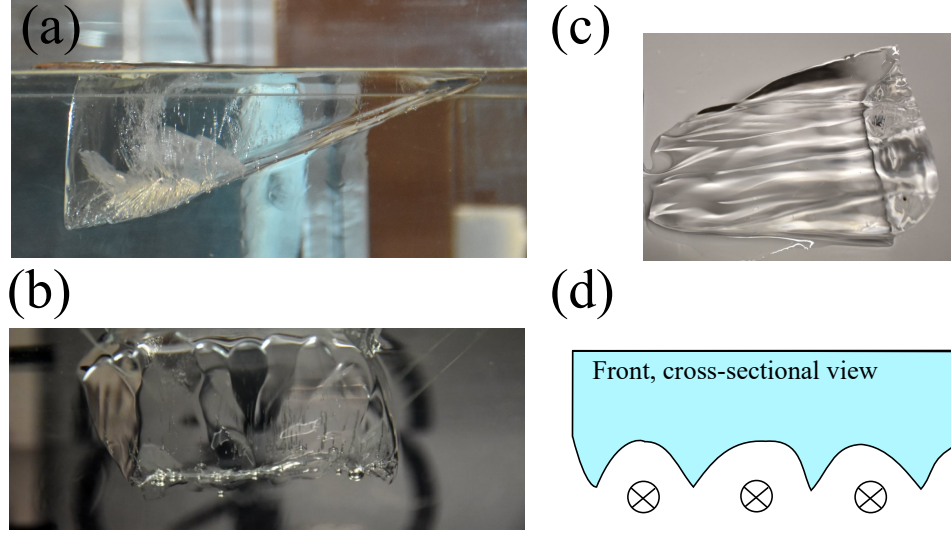


FIG. 6. (a) Image of an ice block corresponding to Data Set **L** ($L = 176$ mm, $\theta = 19.5^\circ$). (b-c) After few minutes, grooves are formed nearly aligned along the length of the block. (b) View from the bottom of the water tank (after about 8 minutes in water), when the ice block is moving in the direction of the observer. (c) Upside down image of the block when it is removed from the water after being immersed over approximately 11 minutes. The typical groove width and depth are about 2 cm and 5 mm, respectively. (d) Schematic cross section of the block illustrating the engh-wise grooves that appear over time in the ice block. The grooves can channel plumes when they are sufficiently deep, leading to further melting and amplification of the groove structure [15].

Dynamics of a symmetric horizontal block

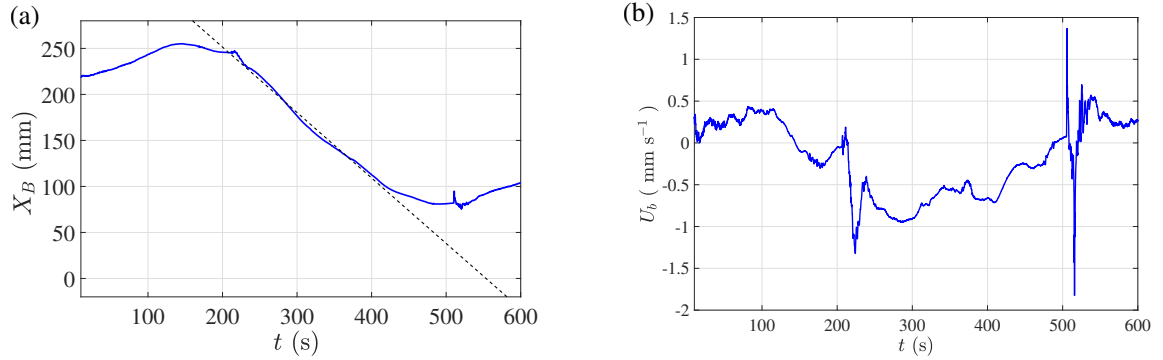


FIG. 7. (a) The horizontal position of a symmetric ice block constrained to move along the horizontal axis. ($T_b = 20.1^\circ\text{C}$). (See corresponding MovieS3.mp4.) The block dimensions: $100 \times 40 \times 40$ mm³, $\theta = 0^\circ$. (b) The corresponding velocity (averaged over 10 s). We observe a slow motion of the block. The block capsizes at $t = 210$ s and $t = 506$ s leading to a sudden change in the convection flow, which can change the direction of the horizontal velocity.

Stability analysis of wedge blocks

The mechanical equilibrium of our ice blocks is reached after few oscillations over a few seconds when the centers of gravity and buoyancy are vertically aligned. In our right angle triangular prism geometry, the hypotenuse is immersed in the fluid at equilibrium, whereas the second longest side of the right triangle emerges slightly above water as shown for example in Fig. 6 in Section . To predict orientation of an ice block floating in water, we perform a 2D numerical analysis. We evaluate the position of the water surface and the position of the center of gravity and center of buoyancy starting from the initial block orientation where the surface of the longest side is aligned with the water surface. If they are not vertically aligned, a small rotation is applied and the level of the water surface is reevaluated. After few iterations, the final block disposition is reached. Numerically, we find the largest inclination for an isosceles right triangle is of 39.6° . Therefore, the possible range of the inclination θ lies between 0° and 39.6° . Few examples of the procedure is illustrated in Fig. 8. For the example of an ice block with dimensions $100 \times 100 \times 50 \text{ mm}^3$, the inclination initially of 25.6° becomes at mechanical equilibrium 24.3° .

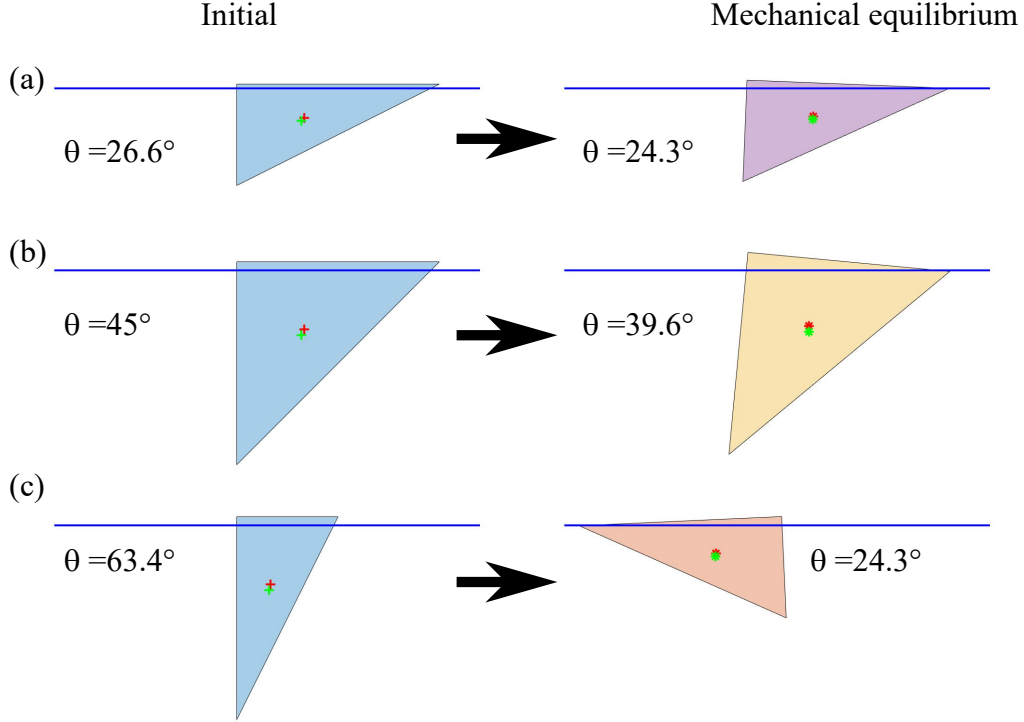


FIG. 8. Numerical analysis of stability of wedge ice blocks. (a) $L_h \times H = 100 \times 50$ (dimensionless units). (b) $L_h \times H = 100 \times 100$. (c) $L_h \times H = 50 \times 100$. The initial and final position of the center of mass and buoyancy are denoted with green and red markers, respectively.

Effect of inclination angle on the terminal velocity

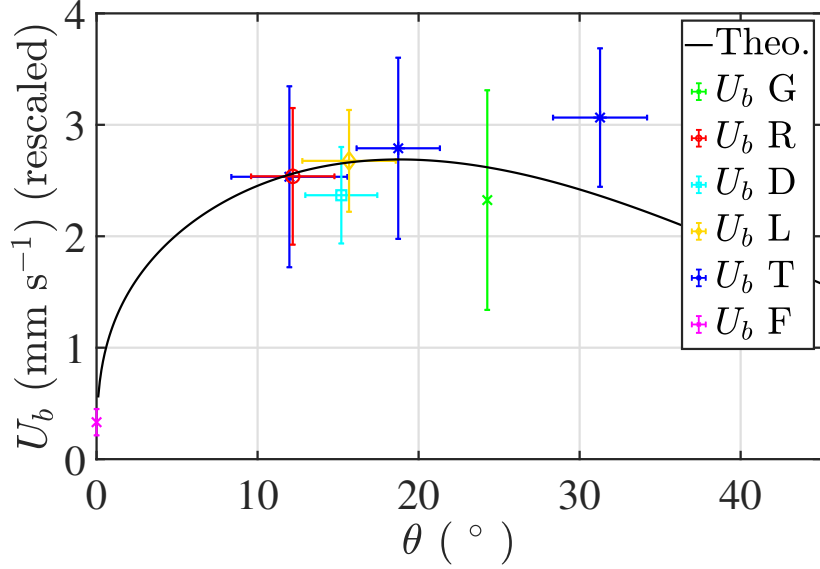


FIG. 9. U_b as a function of the inclination of the bottom surface of the ice block θ and comparison with model. The values of U_b are rescaled in, according to the theoretical model in order to compare experiments with different block properties. $U_{b,G}$, Dimensions: $100 \times 100 \times 50 \text{ mm}^3$, $\theta \approx 24^\circ$, variable temperature varied. Letters refer to Data set listed in Section . The error bars show the average value and \pm the standard deviation. We note for the data set **F** ($U_{b,F}$) for which $\theta \approx 0^\circ$, that $U_b \approx 0$. For the other data sets, we observe a weak dependency with θ in agreement with the theoretical model.

Propulsion model for ice melting in fresh water

Melting driven by thermal convection

In this section, we further discuss the propulsion model of an asymmetric block melting in bath water at a temperature which is above the temperature where the density of water is maximum. We evaluate the melting rate of a floating ice block when the melting is driven by thermal convection and the water bath temperature T_b is greater than $T_c = 3.98^\circ \text{C}$, the temperature where the water density is maximum. To our knowledge, only the work of Keitzl et al. [17] investigates experimentally and numerically the melting of ice in fresh water for a flat ice roof suspended above a water bath. These authors also derived a scaling law for the melting rate driven by thermal convection. However, their model is arbitrarily calibrated using numerical simulations. We propose here a simpler model to predict the melting rate, under the conditions of our experiments in fresh water. Then, the water density has a non-monotonic dependence on temperature T , and can be modeled by a quadratic polynomial function [17]:

$$\rho = \rho_c [1 - \beta (T - T_c)^2], \quad (3)$$

where $\rho_c = 999.96 \text{ kg m}^{-3}$ is the maximal water density at temperature $T_c = 3.98^\circ \text{C}$ and coefficient $\beta = 7 \times 10^{-6} \text{ K}^{-2}$.

We consider an inclined ice block with a volume which is much smaller than the volume of the water bath and assume that the bath temperature sufficiently far from the block is T_b . We suppose that the ice block temperature T_i is at the ice melting temperature $T_m = 0^\circ \text{C}$. As the latent heat of melting is $\mathcal{L} = 333.5 \text{ kJ kg}^{-1}$ and the heat capacity of ice is $C_{p,i} = 2110 \text{ J kg}^{-3} \text{ K}^{-1}$, the energy required to heat the ice block at the melting temperature (if its initial temperature is below 0°C) is negligible for an initial temperature of the ice block larger than -15°C . In addition, the ice blocks are allowed to rest in our experiments for at least 10 minutes after removal from the freezer. Because the ice diffusivity is $\kappa_{ice} = 1.11 \times 10^{-6} \text{ m}^2 \text{ s}^{-1}$, the temperature typically diffuses over a distance $\sqrt{\kappa_{ice} \tau_{rest}} \approx 26 \text{ mm}$. Therefore, for ice blocks that are a few tens of centimeters in size, the block temperature at the beginning of an experiment can be assumed to be approximately T_m .

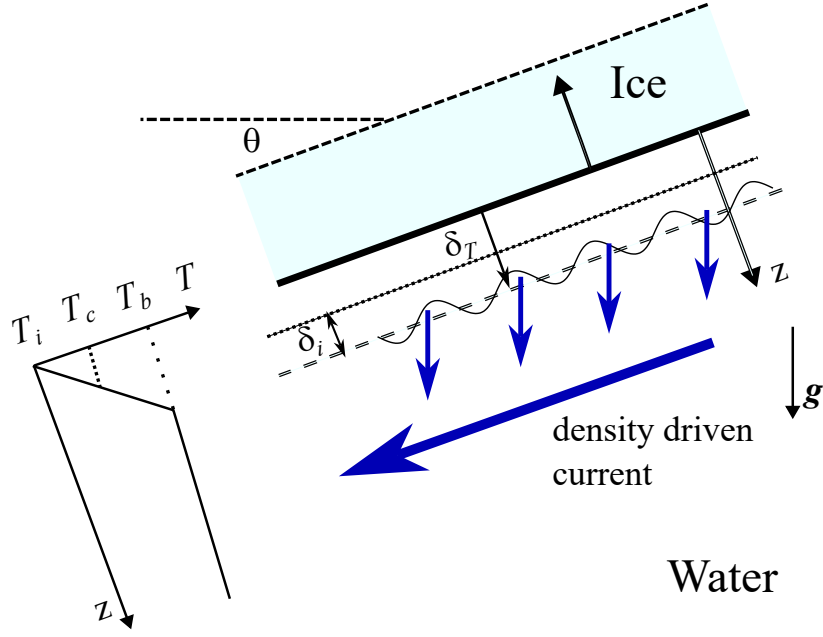


FIG. 10. Schematic of the melting process of ice in water when driven below by thermal convection. In steady melting regime, the thermal boundary layer has a constant thickness δ_T . We simplify the temperature profile to be linear between the ice temperature T_i corresponding to the melting temperature $T_m = 0^\circ \text{C}$ and the bath temperature T_b . When δ_T becomes sufficiently thick, the layer is destabilized by gravity and emits plumes which then sink. These plumes feed a gravity current that moves along the inclined surface with velocity \mathbf{v} . However, as the water density is maximal at $T = T_c$, we consider the instability of the layer of thickness δ_i , which is at a temperature between T_c and T_b to obtain an estimate of δ_T .

For $T_b > T_c$, the cold water close to the ice block is denser than the warmer bath water and this temperature difference drives a convection flow. Under steady state conditions, we assume turbulent thermal convection, *i.e.* on average the temperature change is localized to a thin thermal boundary layer of thickness δ_T , where the temperature increases from T_i to T_b as illustrated in Fig. 10. To simplify the modeling, we suppose a linear temperature profile. The heat transport is diffusive in the boundary layer and convective outside. In the turbulent region below, the sinking plumes and upwelling flow transfer the heat efficiently. Due to the inclination of the block, the convection flow self-organizes into a current of characteristic velocity \mathbf{v} on the scale of the ice block, which escapes the control volume with a velocity \mathbf{v}_p (see Fig. 2(a) in the main document). This directed flow provides the mechanism for the propulsion.

We consider that the melting rate, *i.e.* the velocity v_m of the solid/liquid interface is controlled by the convection flow in the water phase. We denote z as the coordinate normal to the melting interface and z_c as the distance to where $T = T_c$. Then, ρ is below ρ_c over $0 < z < z_c$, where $T_i < T < T_c$, and thus the layer of fluid is stable relatively to gravity. In contrast, the domain $z_c < z < \delta_T$ is denser than the bath at the density $\rho(T_b)$ and could be subjected to convection instability. Assuming a linear temperature profile, we have $z_c = \delta_T (T_c - T_i) / (T_b - T_i)$ and consequently the thickness of the unstable layer is $\delta_i = \delta_T - z_c = \delta_T (T_b - T_c) / (T_b - T_i)$. We evaluate the density contrast $\Delta\rho$ between the fluid at T_c and the fluid at T_b as:

$$\frac{\Delta\rho}{\rho} = 2 \left(\frac{\rho(T_c) - \rho(T_b)}{\rho(T_c) + \rho(T_b)} \right). \quad (4)$$

If $\Delta\rho$ is sufficiently high, a Rayleigh-Bénard instability will be triggered. According to previous studies in geometries with semi-infinite extent under steady state conditions [19–21], the thickness of the boundary layer remains on average close to the critical value corresponding to the onset of the Rayleigh-Bénard instability. From the definition of the Rayleigh number Ra and assuming $Ra = Ra_c$, we then obtain:

$$Ra_c = \frac{\Delta\rho g \cos \theta \delta_i^3}{\rho \kappa \nu}, \quad (5)$$

where $g \cos \theta$ is the gravity acceleration projected along the z coordinate, κ the thermal diffusivity and ν the kinematic viscosity. To obtain a simple estimate, we use the parameter values from Keitzl, *et al.* [17], where the temperature

dependencies are neglected. Between $T = 0^\circ\text{C}$ and $T = 40^\circ\text{C}$, κ changes about 10% and we take $\kappa = 1.33 \times 10^{-7} \text{ m}^2 \text{ s}^{-1}$. However, the decrease in ν with temperature is more significant because $\nu = 1.79 \times 10^{-6} \text{ m}^2 \text{ s}^{-1}$ at $T = 0^\circ \text{C}$, $\nu = 1.58 \times 10^{-6} \text{ m}^2 \text{ s}^{-1}$ at $T = 4^\circ \text{C}$ and $\nu = 1.00 \times 10^{-6} \text{ m}^2 \text{ s}^{-1}$ at $T = 20^\circ \text{C}$ [9]. Accordingly, the thermal Prandtl number in water $Pr = \nu/\kappa$, and is about 13.5 at $T = 0^\circ \text{C}$, $Pr = 11.9$ at $T = 4^\circ\text{C}$, and $Pr = 7.5$ at 20°C . To simplify, we choose to use the average value of ν between T_c and T_b .

Between the two stress-free surfaces, the value of Ra_c is equal to $24/4\pi^4 \approx 658$ [23]. Consequently, we determine δ_T as:

$$\delta_T = \frac{T_b - T_i}{T_b - T_c} \delta_i, \quad \text{with} \quad \delta_i = \left(\frac{Ra_c \kappa \nu}{g \cos \theta} \right)^{1/3} \left(\frac{\Delta \rho}{\rho} \right)^{-1/3}. \quad (6)$$

For $T_b = 20^\circ \text{C}$ and $\theta = 26.5^\circ \text{C}$, $\nu = (\nu(T_c) + \nu(T_b))/2 = 1.29 \times 10^{-6} \text{ m}^2 \text{ s}^{-1}$ and $\Delta \rho/\rho \approx \beta (T_b - T_c)^2 \approx 1.80 \times 10^{-3}$, we find $\delta_i \approx 1.93 \text{ mm}$ and $\delta_T \approx 2.40 \text{ mm}$.

Variations of the fluid properties can be taken into account using empirical correlations available in the literature. We use here Bigg's relation [18] for the density of fresh water as a function of temperature. The experimental and numerical study by Du, *et al.* [30] for freezing of salt water provide correlation laws, in particular for the viscosity and the thermal diffusivity. With these more accurate values of the fluid properties, we find $\delta_T \approx 2.44 \text{ mm}$, which is a small correction to the previous estimated value 2.40 mm . The wavelength at the marginal instability is of order $3\delta_T$ [23], which gives a typical plume size of 7.5 mm . This length is significantly larger than the plumes caused by dissolution of salt or sugar in water which are approximately 0.33 mm and 1 mm , respectively [8, 21, 22].

Then, the melting velocity v_m (defined positive) is given by the Stefan condition [24] at the melting interface with the hypothesis of negligible heat flux in the ice:

$$\rho_{ice} \mathcal{L} v_m = \rho(T_i) c_p \kappa \left. \frac{\partial T}{\partial z} \right|_{z=0}, \quad (7)$$

where $\mathcal{L} \approx 3.33 \times 10^5 \text{ J kg}^{-1}$ is the latent heat of melting ice into water per mass unit at ambient atmospheric pressure and zero salinity and $c_p \approx 4200 \text{ J K}^{-1} \text{ kg}^{-1}$ is the heat capacity of liquid water at the melting temperature T_i . The melting rate becomes:

$$v_m = \frac{\rho(T_i) c_p \kappa}{\rho_{ice} \mathcal{L}} \left. \frac{\partial T}{\partial z} \right|_{z=0}. \quad (8)$$

This velocity can be then estimated with the assumption of linear profile of the temperature, *i.e.* the thermal gradient is linearized in the thermal boundary layer and taken equal to $(T_b - T_i)/\delta_T$ using the value of δ_T from Eq. 6:

$$v_m = \frac{\rho(T_i) c_p \kappa}{\rho_{ice} \mathcal{L}} \frac{T_b - T_i}{\delta_T}, \quad (9)$$

$$v_m = \frac{\rho(T_i)}{\rho_{ice}} St_b (Ra_c Pr)^{-1/3} \left(\frac{\Delta \rho}{\rho} \right)^{1/3} (g \cos \theta \kappa)^{1/3}. \quad (10)$$

Where, we have introduced a Stephan number, $St_b = \frac{c_p (T_b - T_c)}{\mathcal{L}}$ which compares the energy required to cool the water bath to the latent energy. Furthermore, $\frac{\Delta \rho}{\rho}$ is given by Eq. (4), and for $T_b \approx 20^\circ \text{C}$, $St_b \approx 0.2$, the large latent heat of the water-ice transition results in a relatively small melting velocity. In Eq. (10) all the factors are dimensionless, except for the characteristic velocity $(\kappa g)^{1/3}$, which is equal to 10.9 mm s^{-1} . After nondimensionalizing Eq. (10), and using a characteristic length scale L^* large compared to δ_T , it can be shown that the dimensionless thermal flux the Nusselt number Nu is proportional to the Rayleigh number to the power $1/3$. In the general context of thermal convection, this scaling corresponds to the regime where the heat flux is controlled by the thermal boundary layer [19, 31, 32].

The melting rate given by Eq. (10) provides the correct order of magnitude of about few ten microns per second at about $T_b = 20^\circ \text{C}$ and gives a scaling law very close to the prediction of Keitzl *et al.* [17], except close to T_c (see Fig. 11). With complementary measurements (see Sec.), we calibrate the result of Eq. (10) by multiplying it by a fitting constant $\Gamma = 2.187 \approx 2.2$. With this prefactor, as illustrated in Fig. 11, Γv_m is relatively close to the prediction of Keitzl *et al.* [17], although Γv_m is slightly higher for temperature above 10°C . However, the work of Keitzl *et al.* has been tested experimentally only for temperatures ranging from 4.5 to 14.8°C .

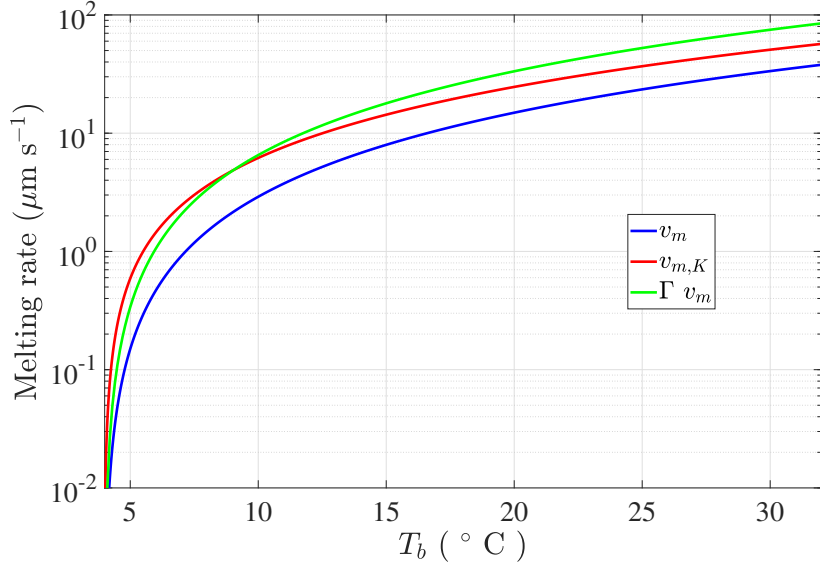


FIG. 11. Theoretical melting velocity or melting rate as a function of the temperature of the bath T_b (fresh water). v_m corresponds to Eq. (10), and $v_{m,K}$ to Keitzl, *et al.* [17] after using $g \cos \theta$ with $\theta = 24^\circ$. $v_{m,K}$ is somewhat higher compared with v_m . By multiplying v_m by the fitting constant $\Gamma = 2.187 \approx 2.2$ (see Sec.), $\Gamma = 2.187 \approx 2.2$ is closer to $v_{m,K}$.

Buoyancy current and terminal velocity

To estimate the propulsion of the floating ice block, we adapt the model derived for inclined dissolving plates in Chaigne *et al.* [8]. According to that work, the convection current below the inclined melting block produces by reaction a propulsion force F_c . By performing a momentum balance in the control volume shown in the schematics of the main text Fig. 3(a), one obtains:

$$F_c \approx \rho_b \frac{W}{2} \delta_x v_p^2 \sin \theta \cos \theta, \quad (11)$$

where v_p is the magnitude of the convection current which exits the control volume, W is the width of the ice block and $\delta_x = \frac{1}{2} \cos^2 \theta L$ is the length over which the flow is ejected. When the terminal velocity U_b is reached, the propulsion force is balanced by the the inertial drag. Then,

$$U_b = \sqrt{\frac{\sin 2\theta \delta_x}{2 C_d L_A}} v_p, \quad (12)$$

where C_d is the drag coefficient of the ice block, and $L_A \approx L \sin \theta$ is the projected length.

Next, we evaluate v_p . The heat extracted from the bath to melt the ice block cools the current from its tip to its back. Consequently, at the location where the fluid exits the control volume the temperature of the fluid \hat{T}_b is lower than T_b . Because T_b is greater than T_c , the resulting density difference accelerates the current under the action of gravity.

To determine the density increase $\hat{\rho}_b - \rho_b$ due to the cooling, we write the energy balance in a fluid layer of thickness δ_v below the melting block, moving with velocity \mathbf{v}_p directed parallel to the inclined wall. Noting that the energy flux is controlled by the melting rate and that the fluid outside the thin thermal boundary layer is well stirred, we have to first order because of energy conservation,

$$\rho_b v_p \delta_v C_p (\hat{T}_b - T_b) = -\rho_{ice} \mathcal{L} L \hat{v}_m, \quad (13)$$

with $C_p \approx 4200 \text{ J kg}^{-3} \text{ K}^{-1}$, the heat capacity of water at the bath temperature and $\hat{v}_m = \Gamma v_m$ is the adjusted melt rate ($\Gamma = 2.2$). Thus, the temperature below the block becomes,

$$\hat{T}_b - T_b = -\frac{\rho_{ice}}{\rho_b} \frac{\hat{v}_m}{v_p} \frac{L}{\delta_v} \frac{\mathcal{L}}{C_p}. \quad (14)$$

Then, using Eq. 3 to evaluate the corresponding density change, we have,

$$\hat{\rho}_b - \rho_b = -\rho_c \beta (\hat{T}_b - T_b) \left[(\hat{T}_b - T_b) + 2(T_b - T_c) \right]. \quad (15)$$

For small temperature difference compared to $T_b - T_c$, $\hat{\rho}_b - \rho_b \approx -\rho_c \beta 2 (\hat{T}_b - T_b) (T_b - T_c)$ and we obtain,

$$\hat{\rho}_b - \rho_b = \frac{\rho_{ice} \rho_c \beta 2 (T_b - T_c) \mathcal{L}}{\rho_b C_p} \frac{L \hat{v}_m}{\delta_v v_p}. \quad (16)$$

Practically, this approximation $\hat{\rho}_b$ is well verified. The coefficient β can be also obtained from a fit of the more precise correlation between the water density and the temperature. Henceforth, we use Bigg's formula for fresh water [18].

As in [8], the velocity of the gravity driven current is then set by the balance between inertial drag of dimensionless coefficient f_D and gravity force due to the density increase given by Eq. 16,

$$(\hat{\rho}_b - \rho_b) g L \sin \theta = f_D \rho_b \frac{L}{\delta_v} v_p^2. \quad (17)$$

Consequently, we obtain the relation between the melting rate $\hat{v}_m = \Gamma v_m$ and the magnitude of the convection current v_p ,

$$v_p = \mu_p \left(\frac{2 \beta (T_b - T_c) \mathcal{L}}{C_p} \frac{\rho_c \rho_{ice} g L \sin \theta \Gamma v_m}{\rho_b^2} \right)^{1/3}, \quad (18)$$

where $\mu_p = (f_D)^{-1/3} = 0.2 + 0.38 \cos^2 \theta$, where we use the empirical law discussed by Chaigne, *et al* [8] in Supplementary Information Section 11. Typically, for $T_b = 20^\circ \text{C}$ and $\theta = 26.5^\circ$, v_p is an order of few millimeter per second. Then, as $(v_m L)/(v_p \delta_v) \approx v_m/v_p \approx 100$, the contribution of the meltwater to the water flow can be neglected. The result of Eq. 18 is then inserted in Eq. 12 to calculate the terminal velocity for the various experiments in Fig. 2(a) of the main document.

As a remark, we neglect the influence of the propulsion flow in the melting dynamics in modeling our experiments. Indeed, the propulsion velocities appear too small to efficiently shear the thermal boundary layer and increase the melting rate. The Richardson number compares the magnitude of the buoyancy force to the inertial force caused the flow,

$$Ri = \frac{\Delta \rho g \mathcal{D}}{\rho \mathcal{V}^2}, \quad (19)$$

where \mathcal{D} and \mathcal{V} are characteristic length and velocity, respectively. For our experiments, we take $\Delta \rho/\rho = \beta (T_b - T_c)^2$, $\mathcal{D} = L$ and $\mathcal{V} = v_p \approx U_b$. With $T_b = 20^\circ \text{C}$, $L = 0.2 \text{ m}$ and $U_b = 5 \text{ mm s}^{-1}$, we find $Ri \approx 140$. This value means that the buoyancy forces are dominant compared to the shear flow due to the gravity driven current or the block motion. Consequently, we neglect the possible feedback of the ice block velocity on the melting rate.

First order estimation of the terminal propulsion velocity

In order, to obtain a more general estimation of the terminal velocity of order one $U_{b,sc}$, we can remove the angular dependency and estimate the melting rate by approximating the Stefan condition given by Eq. 9, as

$$v_m \sim \frac{\rho(T_i) C_p \kappa (T_b - T_i)}{\rho_i L \delta_T} = \frac{\rho(T_i) C_p \kappa (T_b - T_c)}{\rho_i \mathcal{L} \delta_i}. \quad (20)$$

By substituting this expression in Eq. 18 and noting that to first order $U_b \sim v_p$, we obtain,

$$U_{b,sc} \sim (\beta (T_b - T_c)^2)^{1/3} \left(\frac{\rho(T_i) \rho_c}{\rho_b^2} \right)^{1/3} \left(\frac{L}{\delta_i} \right)^{1/3} (\kappa g)^{1/3}. \quad (21)$$

We note that the ratio \mathcal{L}/C_p is absent. According to the simple model, the boat velocity depend neither on the latent heat \mathcal{L} , nor on the ice density ρ_{ice} . The presence of trapped bubbles thus cannot be expected to significantly change the observed propulsion velocities.

For $T_b = 20^\circ \text{ C}$ and $L \approx 10 \text{ cm}$, $\beta (T_b - T_c)^2$ is of order $1.81. \times 10^{-3}$, whereas $(\rho(T_i) \rho_c)/\rho_b^2$ is approximately equal to 1 and the ratio of length L/δ_i is roughly about 50. The only dimensional factor is the characteristic velocity $(\kappa g)^{1/3} \approx 11 \text{ mm s}^{-1}$. Then, Eq. 21 provides an estimation of the terminal velocity: $U_{b,sc} \sim 5 \text{ mm s}^{-1}$, which is the same order of magnitude as observed in our experiments. As expected, the boat velocity increases with the bath temperature T_b . By combining Eq. 6 and Eq. 21, we find, $U_b \sim (T_b - T_c)^{8/9}$. The terminal ice block velocity is thus nearly proportional to $(T_b - T_c)$. Moreover, according to Eq. 21, U_b increases with the block length as $L^{1/3}$, that is a weak variation with the block size. Finally, the dependency of U_b with the inclination θ is neglected in Eq. 21. However, by combining Eqs. 12, 18 and 10, we find the corresponding angular dependency, which is by construction identical to the one found for the dissolving boats [8]:

$$g(\theta) = \left(\frac{\cos^2 \theta \sin(2\theta)}{\sin \theta} \right)^{1/2} (0.2 + 0.38 \cos^2 \theta) (\sin \theta)^{1/3} (\cos \theta)^{1/9}. \quad (22)$$

In order to compare the measured U_b obtained with different experimental parameter values compared to the theoretical prediction, we perform a rescaling of the value of U_b to include the expected theoretical dependency. We choose as reference parameters, $L_r = 0.1 \text{ m}$, $\theta_s = \text{atan}(5/10) \approx 26.6^\circ$ and $T_{b,s} = 20^\circ \text{ C}$. To test the influence of the bath temperature T_b in Fig. 3 (b) of the main document, the measured values of U_b are thus multiplied by $(L_s/L)^{1/3} \times g(\theta_s)/g(\theta)$. Similarly in Fig. 3 (c), to test the block length, U_b is multiplied by $g(\theta_s)/g(\theta) \left(\frac{T_{b,s} - T_c}{T_b - T_c} \right)^{8/9}$. Finally, to test the inclination θ in Fig. 9, the values of U_b are multiplied by $(L_s/L)^{1/3} \times \left(\frac{T_{b,s} - T_c}{T_b - T_c} \right)^{8/9}$.

Measurement of the melting rate

We perform a set of measurement with inclined blocks to adjust the result of our model predicting the melting rate. Clear ice blocks of dimensions $100 \times 40 \times 100 \text{ mm}^3$ are fixed at a given inclination. The displacement of the bottom interface subjected to a detached thermal convection flow is monitored with two lighting protocols. First, we use the shadowgraph imaging, already presented to visualize the convection flow. Secondly, a LED backlight is placed at the back of the glass tank. Although a significant dispersion is present in the measurements, we can estimate the measured melting rate using Eq. 10 multiplied by a factor $\Gamma = 2.187 \approx 2.2$, as shown in Fig. . Nevertheless, the expected decrease of the melting rate predicted by the model close to $\theta = 90^\circ$ is not really observed experimentally. For a vertical ice block, the hypothesis of detached convection flow made of sinking plumes is likely not sufficient to describe the melting process, leading to an underestimation. Finally, we do not find in the literature an experimental study measuring the melting rate of inclined block for a bath temperature close to 20° C .

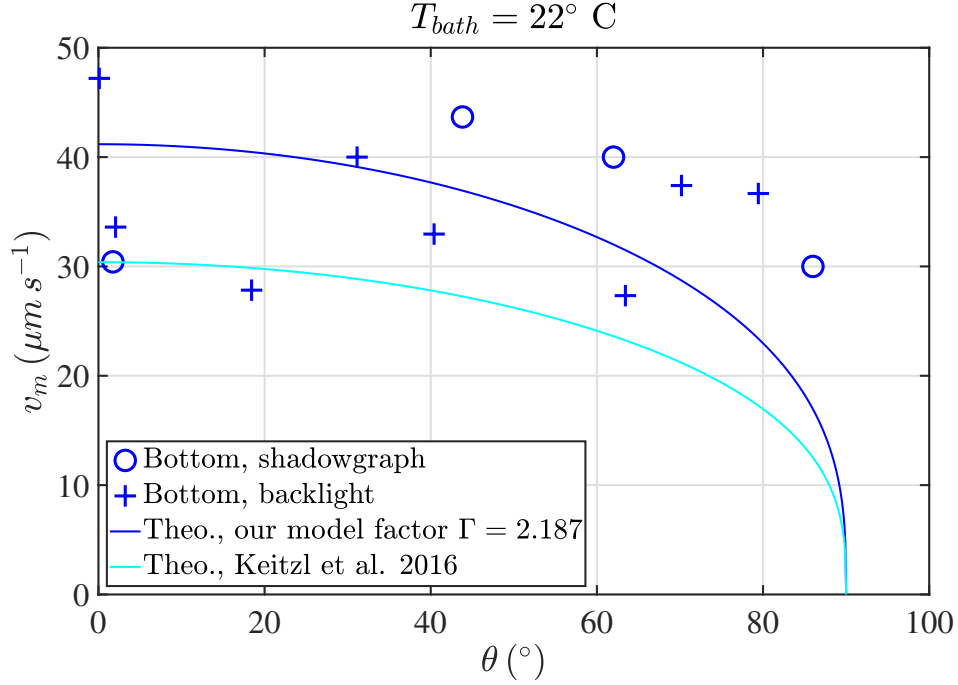


FIG. 12. Experimental measurements of the melting rate v_m at the bottom surface of an ice block as a function of its inclination in fresh water. These measurements enable us to calibrate the ice melting model in fresh water. The blocks are held at rest, $T_b = 22^\circ \text{ C}$ and their dimensions correspond to Data set F (clear ice).

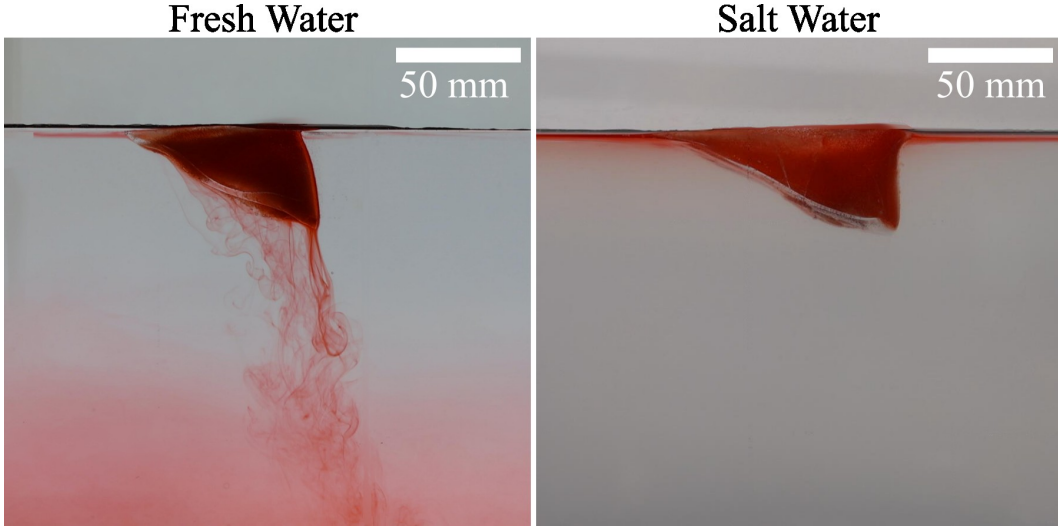


FIG. 13. An ice block ($L_h \times W \times H \approx 121 \times 80 \times 50 \text{ mm}^3$ and $\theta \approx 25^\circ$) dyed with red food color to track melt water in clear fresh water and in salt water (35 g salt per kg of water). The snapshots were taken about 4.5 minutes after placing the ice block in the bath ($T_b \approx 22^\circ \text{C}$). The melt water descends to the bottom in fresh water and rises to the surface in salt water because of the relative density difference with the bath.

Melting driven propulsion in salt water

Experiments were performed for salinity (mass of dissolved salt over the mass of liquid) of 0, 5.77, 11.84, 23.72 and 35.00 g kg⁻¹. This last value corresponds to the typical salinity of the ocean. For this set, block sizes of length about $L \approx 210 \text{ mm}$ and $\theta \approx 25^\circ$ were chosen, whereas the bath temperature is about $T_b \approx 23^\circ \text{C}$. We observe a similar propulsion effect with the same order of magnitude of the terminal propulsion velocity U_b as in fresh water. As shown in Fig. 4(a) of the main document, U_b decreases with the salinity. We perform also a complementary experiment with shadowgraph imaging (corresponding to MovieS4 and Fig. 4(b) of the main document) in order to better visualize the convection flow. In that case, the salinity is 31 g kg⁻¹, $L \approx 112 \text{ mm}$, $\theta = 24^\circ$ and $T_b = 24.6^\circ \text{C}$. As reported, we observe a similar translation motion with the same direction than in fresh water. In shadowgraph images, the convection flow corresponding to the cooled salt water put in motion is well visible. However, the thin layer of fresh water produced by the melting is not visible. As the fresh water is less dense than salt water, this layer is expected to move upward by gravity.

To demonstrate the motion of the meltwater layer, we performed complementary experiments with ice blocks that were dyed with red food coloring. The resulting image is shown in Fig. 13 and compared to the case of fresh water. The meltwater produced by melting of the ice blocks moves thus at the free surface of the tank.

To model the salt water experiments where the melt water rises and the bath water below descends, we consider an inverted inclined ice surface melting in salt water. We use the Gibbs-SeaWater (GSW) Oceanographic Toolbox of the Thermodynamic Equation of Seawater 2010 (TEOS 2010) [33] to incorporate the density changes of salt water as a function of temperature. We suppose laminar melt flow, *i.e.* the fresh melt water is not mixed with the salt water of the bath, because the diffusion of salt in the melt water layer is slow over the time scale of flow along the inclined surface. Therefore, the melting temperature is always assumed to be equal to 0°C . As the melt water layer is lighter, it should be driven upwards by a laminar convection flow, due to the density difference caused by the salinity. Then, we assume that melting feeds the meltwater flow, which has a half-Poiseuille (or Nusselt) profile of thickness $h(x')$ (see Fig. 14),

$$w = K z (2h(x') - y') \quad \text{with } K = \frac{g \sin \theta \Delta \rho}{2 \rho \nu}. \quad (23)$$

w is the velocity parallel to the block, but a velocity perpendicular u to the block is generated by the melting. For a zero divergence flow,

$$\frac{\partial u}{\partial y'} = -\frac{\partial w}{\partial x'} = -2K y' \frac{dh}{dy'}.$$

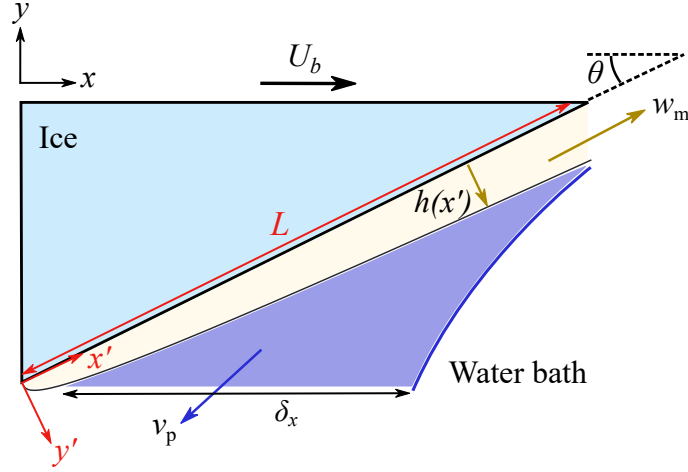


FIG. 14. Schematic of a melting ice block self-propelling with velocity U_b while floating in salt water. Below the right angle prism of ice, two layers of fluid coexist and behave differently. In contact with the ice, a thin layer of pure melt water is accelerated upwards due to its smaller density than that of salt water. Its thickness h and velocity w increase along the x' axis, parallel to the hypotenuse. Further away from the ice, a layer of salt water is cooled because of the melting of the block. It is therefore denser than the bath, unstable by gravity, and it flows downwards and backwards with a typical velocity v_p and a typical thickness δ_x .

Because of mass conservation of the melt water, and with the approximation that ice and liquid water have the same density (error about 9%), the normal velocity is related to the melting velocity by $u(x, 0) = v_m$. We obtain for a block of length x ,

$$h(x') = \left(\frac{3 v_m x'}{2 K} \right)^{1/3}. \quad (24)$$

Moreover, the velocity of the meltwater current reads $\langle w \rangle_z = \frac{2}{3} K (h(x))^2$. With a typical melting rate of $v_m \sim 30 \times 10^{-6} \text{ m s}^{-1}$ at 20° C and a block of length $L = 20 \text{ cm}$, we find $h_{melt} \approx 0.5 \text{ mm}$, $w_{melt} \approx 10 \text{ mm s}^{-1}$ and a Reynolds number $Re = \frac{w_{melt} h_{melt}}{\nu} \approx 5$.

Propulsion in salt water due to the cooling of the bath

Then, we assume, that in warm water, the melting rate is driven by thermal convection, like for the previous case in fresh water. The model is identical to the one presented in Sec. with the incorporation of the density dependence with salinity, except in the calculation of the melting rate. The physical parameters take into account the salinity dependence. For sufficient salinity (above roughly 18 g kg^{-1}) of water, the density maximum of liquid water disappears (monotonic decrease of $\rho(T)$) and we assume that the linear thermal boundary layer corresponds to a decreasing density profile. In this last case, all the thermal boundary layer is unstable, that means $\delta_i = \delta_T$ using our previous notations and δ_T is given by the criterion for critical Rayleigh number,

$$\delta_T = \left(\frac{Ra_c \kappa \nu}{g \cos \theta} \right)^{1/3} \left(\frac{\Delta \rho}{\rho} \right)^{-1/3}. \quad (25)$$

Then, the melting rate according to the Stefan condition, reads

$$v_m = \frac{\rho(T_i)}{\rho_{ice}} \frac{c_p \kappa}{\mathcal{L}} \frac{T_b - T_i}{\delta_T}. \quad (26)$$

We use Eq. 6, to determine δ_T . With this model, we find that the bath salinity slightly increases the melting rate, because the density contrast between warm and cold water is enhanced by the salinity.

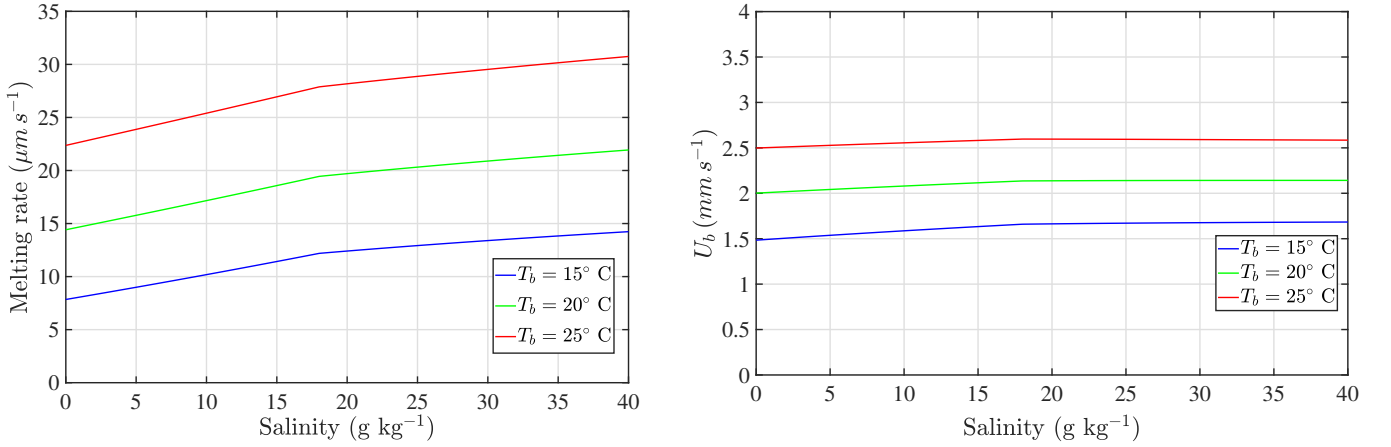


FIG. 15. **Left**, melting velocity or melting rate as a function of the bath salinity. The melting rate is evaluated using Eq. (26). We find with our model, that the bath salinity increases the melting rate. **Right**, ice propulsion velocity as a function of bath salinity for an ice block of length 110 mm and inclination 23° and few selected bath temperatures T_b .

Then the propulsion velocity is obtained by calculating the large scale convection current v_p using Eq. 18, which is proportional to the stationary propulsion velocity U_b according to Eq. 12. We find that salinity should not have a strong influence on the propulsion velocity, as illustrated in Fig. 15. For a salinity close to the one of oceans, we find the strength of the convection current $v_p \approx 3.2 \text{ mm s}^{-1}$. With this model, where the contribution of the fresh meltwater to the propulsion is neglected, the correct order of magnitude is predicted, but the decrease of U_b with the salinity as illustrated in Fig. 4(a) of the main document is not captured.

Competition between the meltwater layer flow and the cooled layer flow

As noted from images obtained of the bath obtained with shadowgraph technique and with dyed ice blocks, a layer of rising fresh water fed by melting ice exists adjacent to the ice block and a layer of descending cooled bath salt water below. As a first approximation, we assume that both layers behave independently. The layer of cooled water, which is unstable, behaves as described in fresh water, except for the fact that the values of the physical parameters change. Then, we assume that the melt layer remains pure (which is reasonable since the time scales associated with diffusion of solute are much larger than the hydrodynamics ones) and is assumed to remain at the melting temperature for sake of simplification. In salt water, this layer is lighter than the surrounding fluid. As demonstrated, it therefore goes up the inclined wall of the ice block while remaining attached to it. Because melt water is continuously added along the block, the thickness $h(x')$ of the melt water layer increases with distance x' along the inclined surface, as illustrated in schematic 14. Its velocity $w(x')$ also increases along x' and the layer is then ejected in the x direction which, by momentum balance, is therefore associated with a net force in the opposite direction. The values of $h(x')$ and $w(x', y')$ according to Eq. 24 and 23 are given by,

$$h(x') = \left(\frac{3\rho_0\nu v_m x'}{\Delta\rho g \sin\theta} \right)^{1/3} \quad \text{and} \quad w(x', y') = \frac{\Delta\rho g \sin\theta h(x')^2}{\rho_0\nu} \left(1 - \frac{y'}{2h(x')} \right) \frac{y'}{h(x')}, \quad (27)$$

with ρ_0 the density of pure water at $T = 20^\circ \text{ C}$ and $\Delta\rho = \rho_b - \rho_0$ the difference in density between salt water at the bath temperature and pure water at the melting temperature.

The contribution F_m of the melt layer to the force exerted by the fluid on the solid can then be obtained by momentum balance, with a similar reasoning as the one used to obtain the contribution of the cooled layer,

$$\mathbf{F}_m = -W \int_0^{h(L)} \rho_0 w(L, y')^2 dy' \mathbf{e}_{x'} = -\frac{2}{3} W \rho_0 h(L) w(L, h(L))^2 \mathbf{e}_{x'}, \quad (28)$$

where $\mathbf{e}_{x'}$ is a unit vector along x' -axis. Then, we obtain the horizontal component of the force in the x direction and using Eq. 27,

$$F_m = -\cos\theta \rho_0 W \left(\frac{\Delta\rho g \sin\theta}{3\rho_0\nu} \right)^{1/3} (v_m L)^{5/3}. \quad (29)$$

The terminal propulsion velocity then expresses the balance between drag, this force F_m due to the melt layer and the force F_c due to the cooled layer defined by equation 11.

$$U_{b,thS} = \sqrt{\frac{2(F_c + F_m)}{C_D \rho W L_A}}. \quad (30)$$

Both F_m and F_c are plotted in Fig. 16 for different bath temperatures. It can be seen that, while F_c increases with the salinity for all temperatures, F_m has a strong dependence in salinity and notably changes sign. Indeed, at sufficiently low salinity, the temperature effect on density outweighs the salinity effect and thus the cold, pure melt layer is denser than the warm, salt water of the bath. Then, the melt layer goes down in the same direction as the cooled layer, which induces a positive force in the x direction. On the other hand, above a critical salinity which depends on the bath temperature, the pure melt layer becomes less dense than the warm, salt water (this is the situation drawn on schematic 14 and demonstrated in Fig. 16 Left). The associated force becomes negative in the x direction. As salinity increases, this negative force compensates for the increase in force due to the cooled water layer, but only at temperatures above 20°C. This is roughly consistent with our data obtained for a temperature of 23°C, which shows that U_b decreases with salinity, even though our model underestimates this decrease. This can be explained by the strong assumptions made, in particular the fact that the layer of melt water remains completely independent of the layer of cooled water, neither mixes with it, nor drags part of it upwards.

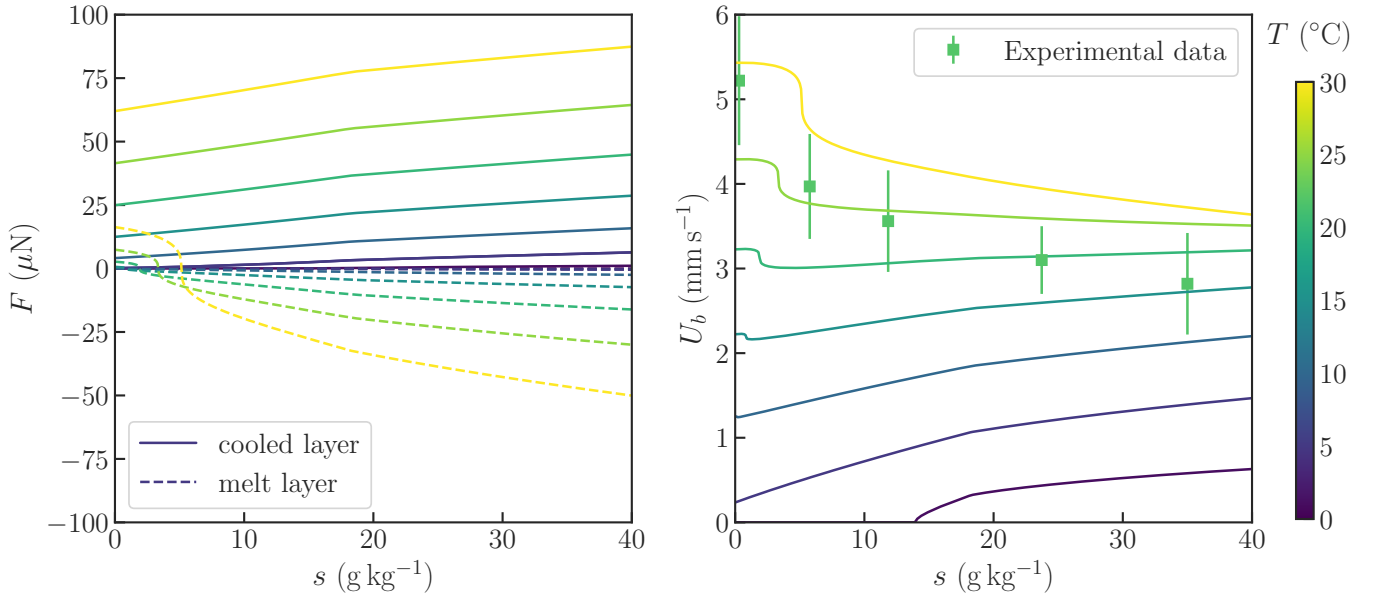


FIG. 16. **Left**, propulsion force in salt water for various bath temperature T_b . Continuous line, F_c contribution of the cooled layer in salt water according to Eq. (11). Dashed line, F_m contribution of the melt layer, Eq. (29). **Right**, ice propulsion velocity U_b as a function of bath salinity for an ice block of length 21 cm and inclination 25° for different bath temperatures T_b , taking into account the contribution of the melt layer. The theoretical estimate is obtained using Eq. (30).